communications physics

A Nature Portfolio journal

Article

https://doi.org/10.1038/s42005-026-02560-4

Synchronization transitions and spike dynamics in a higher-order Kuramoto model with Lévy noise

Dan Zhao [1,2], Jürgen Kurths [1,2], Norbert Marwan [1,3] & Yong Xu [4,5]

Synchronization in complex networks is influenced by higher-order interactions and non-Gaussian perturbations, yet their mechanisms remain unclear. We investigate the synchronization and spike dynamics in a higher-order Kuramoto model subjected to Lévy noise. Using the mean order parameter, mean first-passage time, and basin stability, we identify boundaries distinguishing synchronization and incoherence. The stability index governs the tail heaviness of the probability density function for Lévy noise, while the scale parameter affects the magnitude. Synchronization weakens as the stability index decreases, and even completely disappears when the scale parameter exceeds a critical threshold. By varying coupling, we find bifurcations and hysteresis. Lévy noise smooths the synchronization transitions and requires stronger coupling compared to Gaussian white noise. We then define spikes as extreme excursions of the order parameter and study their statistical and spectral properties. The maximum number of spikes is observed at small-scale parameters. A generalized spectral analysis based on an edit distance algorithm measures the similarity between spike sequences and identifies spike patterns. These findings deepen the understanding of synchronization and extreme events in complex networks driven by non-Gaussian noise.

Synchronization is a universal phenomenon widely observed in natural and engineering systems, including neuronal brain networks[1], biological rhythms[2], ecological networks[3] and power grids[4]. It provides insights into how collective order emerges from complex interactions among individual units[5,6]. The Kuramoto model serves as a fundamental mathematical framework for analyzing synchronization phenomena, describing the interactions among oscillators in a reduced and effective form. Its clear characteristics of synchronization transitions make it particularly beneficial for designing resilient networks and effectively suppressing oscillations in real world networks[7–10].

However, the classical Kuramoto model considers only pairwise interactions, while many real-world systems rely on higher-order couplings, including triadic and even higher-order interactions, significantly enriching the dynamical behaviors [11–13]. Recent studies have identified several distinctive synchronization phenomena induced by higher-order couplings, such as abrupt desynchronization transitions, no synchronization, and multistability[14,15]. Besides, Millán et al.[16] present an explosive synchronization transition in a higher-order Kuramoto model. Clustering and abrupt desynchronization transitions are investigated arising from a three-way interaction in the Kuramoto model[17]. Kundu et al.[18] demonstrate that higher-order interactions in nonlocally coupled identical Kuramoto oscillators promote the emergence of chimera states without a nonzero phase lag. Complex spatiotemporal dynamics are illustrated on spatially embedded networks driven by local triadic interactions[19], resulting in abundant topological patterns. Furthermore, higher-order interactions have been shown to enhance the linear stability of synchronized states, while simultaneously shrinking their basins of attraction[20], revealing a fundamental trade-off between local stability and global robustness. These findings highlight the significant role of non-pairwise interactions in complex dynamical behaviors. Understanding these dynamics is important for practical applications, including the development of resilient power grids[21], the engineering of robust communication infrastructures[22,23], and the elucidation of intricate biological rhythms[24,25].

In addition to interactions among oscillators, many real systems are always influenced by stochastic excitation[26–29]. Gaussian white noise is commonly used to model such external disturbances[30,31]. Many scholars

[1]Potsdam Institute for Climate Impact Research (PIK), Member of the Leibniz Association, Potsdam, Germany. [2]Department of Physics, Humboldt University Berlin, Berlin, Germany. [3]Institute of Physics and Astronomy, University of Potsdam, Potsdam, Germany. [4]School of Mathematics and Statistics, Northwestern Polytechnical University, Xi'an, China. [5]MOE Key Laboratory for Complexity Science in Aerospace, Northwestern Polytechnical University, Xi'an, China.
e-mail: hsux3@nwpu.edu.cn

have investigated the collective dynamical behaviors of higher-order oscillators under Gaussian white or colored noise, revealing richer dynamical phenomena compared to deterministic systems[32–35]. We have previously investigated the heavy-tailed behavior of probability density functions (PDFs) in generalized Duffing systems driven by irregular periodic excitations under Gaussian colored noise, and found that stronger noise intensities and shorter correlation times lead to heavier tails[32]. Recently, Marui et al.[35]) investigated synchronization behaviors in higher-order Kuramoto oscillators with simplex interactions driven by Gaussian white noise. They find that even extremely weak noise erodes synchronization states, leading to the lifetime of the synchronization state exhibiting an exponentially growing slow decay. However, realistic disturbances often exhibit characteristics different from Gaussian noise, such as large jumps, leading to rare but significantly impactful extreme events. Lévy noise, characterized by heavy-tailed distributions, naturally captures these extreme fluctuations and abrupt perturbations more accurately[36,37]. For example, Liu et al.[37] study stochastic transitions and stochastic resonance in a conceptual airfoil system subjected to non-Gaussian Lévy noise.

Nonetheless, the synchronization dynamics of higher-order Kuramoto models under Lévy noise remain largely unexplored, leaving a basic gap in our understanding of synchronization in complex networks with higher-order interactions. Moreover, Lévy noise often triggers extreme events, such as extreme synchronization events or spike events[27,38], which represent transient, high-coherence states significantly exceeding typical synchronization levels. These extreme events have profound implications for the stability and robustness of real-world systems. Critically, unlike Gaussian fluctuations which act diffusively, the heavy-tailed shocks of Lévy noise may induce fundamentally different transition mechanisms, potentially suppressing the transient coherence that naturally emerges in finite-size systems. Therefore, the present study investigates synchronization dynamics in higher-order Kuramoto models under Lévy noise, exploring how Lévy disturbances and higher-order interactions influence synchronization and spikes.

In this work, we show that Lévy fluctuations impede synchronization and stronger pairwise and higher-order interactions promote synchronization, revealing a critical interplay between higher-order interactions and non-Gaussian stochastic dynamics. Furthermore, we find that the amplitude and frequency of these spikes are enhanced by a lower Lévy noise scale parameter. These spikes also carry distinct statistical signatures of the underlying collective state, evident in their autocorrelation and power spectrum. Specifically, we find that the spike autocorrelation function decays rapidly in the incoherent regime, but exhibits significantly longer persistence during synchronization. Finally, the power spectra of these spiking events show power-law behavior, with underlying periodicities revealed by a windowed spectral analysis.

Results

Model overview

We consider the following higher-order Kuramoto model subject to non-Gaussian Lévy noise. In particular, the phase dynamics of the ith oscillator is governed by[39]

$$\dot{\theta}_i = \omega_i + \frac{K_1}{N}\sum_{j=1}^{N}\sin\left(\theta_j - \theta_i\right) + \frac{K_2}{N^2}\sum_{j=1}^{N}\sum_{k=1}^{N}\sin\left(2\theta_j - \theta_k - \theta_i\right) + \zeta_i(t), \quad (1)$$

in which θ_i is the phase of the ith oscillator and ω_i is the natural frequency of the ith oscillator. N is the total number of oscillators. $i, j = 1, 2, \ldots, N$. K_1 and K_2 are the coupling parameters of pairwise and triadic interaction, respectively. $\zeta_i(t)$ represents non-Gaussian Lévy noise. The natural frequencies $\{\omega_i\}$ are drawn independently from the standard Cauchy distribution, whose PDF is given by

$$g(\omega) = \frac{1}{\pi(\omega^2 + 1)}.$$

Lévy noise $\zeta_i(t)$ is the formal derivative of the Lévy process $L(t)$ to time t. $L(t)$ is expressed by its characteristic function $\phi_{\zeta_i}(t)$[40], namely

$$\phi_{\zeta_i}(t) = \begin{cases} \exp\left\{\iota\mu t - \sigma^\alpha|t|^\alpha\left[1 - \iota\beta\,\mathrm{sgn}(t)\tan\left(\frac{\pi\alpha}{2}\right)\right]\right\}, & \alpha \in (0,1)\cup(1,2], \\ \exp\left\{\iota\mu t - \sigma|t|\left[1 + \iota\beta\,\mathrm{sgn}(t)\frac{2}{\pi}\ln|t|\right]\right\}, & \alpha = 1. \end{cases} \quad (2)$$

In Eq. (2), $\iota = \sqrt{-1}$ is the imaginary unit. α is the stability index and β the skewness index. When $\alpha = 2$, Lévy noise degenerates into Gaussian noise. $\beta > 0$ means a left-skewed PDF, and $\beta < 0$ means a right-skewed PDF. $\beta = 0$ shows the symmetric case. $\mu \geqslant 0$ is the location parameter and σ the scale parameter. So the noise intensity is $D = \sigma^\alpha$.

Here, $\{\omega_i\}$ and $\{\zeta_i(t)\}$ are assumed to be mutually independent. The scale parameter of the standard Cauchy distribution is 1, so that σ plays the role of the dimensionless noise intensity. Unless stated otherwise, we consider finite ensembles with $N = 100$ oscillators. For each parameter set, we generate multiple independent realizations of $\{\omega_i\}$, together with independent noise trajectories and initial conditions. All reported observables are averaged over these realizations.

The macroscopic synchronization level is quantified by the order parameter

$$re^{\iota\Psi} = \frac{1}{N}\sum_{j=1}^{N} e^{\iota\theta_j}, \quad (3)$$

where $r \in [0, 1]$ measures the degree of phase coherence and Ψ is the mean phase.

Basins of attraction in the noise-free case

Considering fixed K_1 and K_2, we focus on the stable and unstable fixed points of the system (1). The nonlinear differential equation of the global order parameter $r(t)$ is as follows[39].

$$\dot{r} = -r + \frac{K_1}{2}\left(r - r^3\right) + \frac{K_2}{2}\left(r^3 - r^5\right). \quad (4)$$

Fixed points are obtained by setting $\dot{r} = 0$, which yields

$$-\frac{r}{2}\left[K_2 r^4 + (K_1 - K_2)r^2 + (2 - K_1)\right] = 0. \quad (5)$$

For $K_1 = 0.8$ and $K_2 = 8.0$, the fixed-point condition above yields three real solutions in $0 \leq r \leq 1$: a stable fixed point $r = 0$, an intermediate unstable fixed point $r = r_u \approx 0.47$, and a non-trivial stable fixed point $r = r_s \approx 0.82 < 1$, representing a coherent state close to full synchrony. Thus, the deterministic dynamics are bistable between the incoherent state $r = 0$ and a partially synchronized coherent state $r = r_s$, separated by the unstable fixed point $r = r_u$. These two stable fixed points represent, respectively, the incoherent state and a coherent state.

By numerically integrating Eq. (4) from various initial conditions $r_0 \in [0, 1]$, we obtain their basins of attraction, as shown in Fig. 1. Different initial conditions lead to two different states, including $r = 0$ and $r = r_s$. Blue markers denote trajectories that converge to the incoherent state $r = 0$, whereas red markers indicate those that approach the coherent state $r = r_s$. The vertical dashed line at $r_0 = r_u \approx 0.47$ marks the separatrix between these two basins. This sharp threshold underlines the system's bistability.

In what follows, considering different K_1 and K_2, the basin of attraction will be calculated, as shown in Fig. S1 (Supplementary Note 1). A bistable region occurs for different K_1 and K_2. The approximate boundary observed in Fig. S1 reflects the effective threshold for the finite-size system to reach synchronization from the given initial conditions.

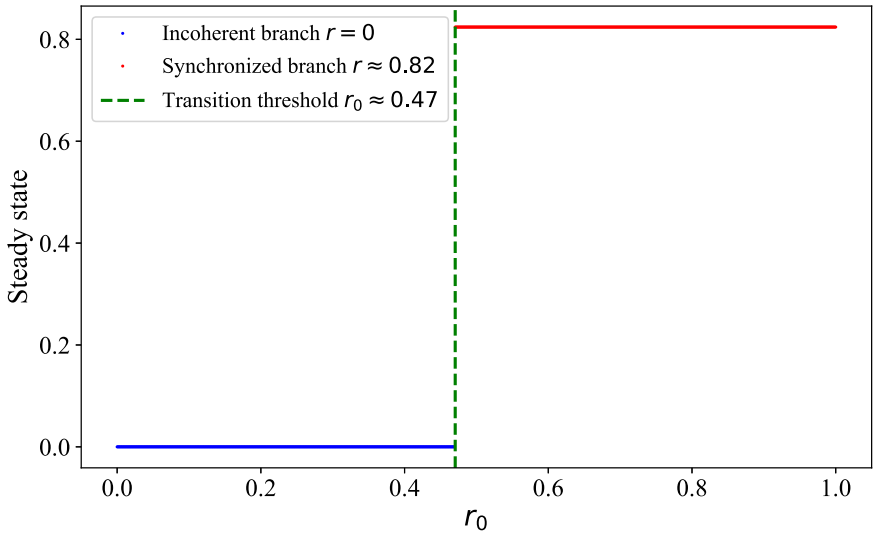

Fig. 1 | The stable and unstable points are given by Eq. (4). The blue branch describes order parameter $r = 0$, while the red branch is $r \approx 0.82$. The green dashed vertical line marks the transition point at the initial condition $r_0 \approx 0.47$, separating the basins of attraction of the two stable steady states.

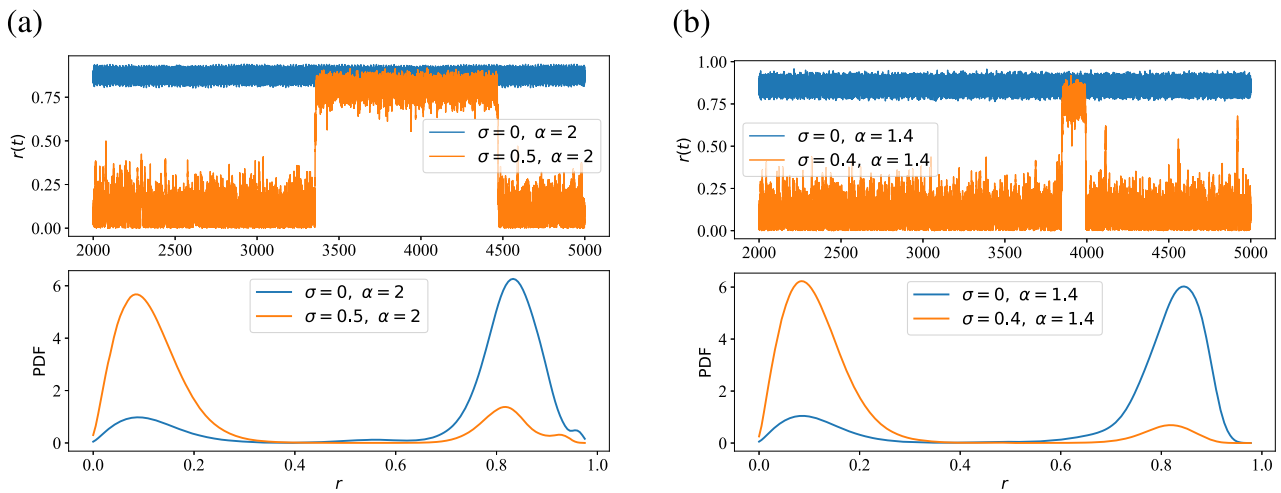

Fig. 2 | Effects of Gaussian and Lévy noise on the dynamics and stationary distribution of the order parameter. In each subfigure, the first row shows the time series of order parameter $r(t)$, and the second row shows the PDF obtained by multiple trajectories. The number of oscillators $N = 100$. Blue curves represent the deterministic case (scale parameter $\sigma = 0$), and orange curves show the stochastic case ($\sigma > 0$). **a** $\sigma = 0.5$, $\alpha = 2$ (orange curves) and $\sigma = 0$, $\alpha = 2$ (blue curves). **b** $\sigma = 0.4$, $\alpha = 1.4$ (orange curves) and $\sigma = 0$, $\alpha = 1.4$ (blue curves).

Based on the analysis of the steady states for different K_1 and K_2, we now proceed to investigate the synchronization transition of the system (1) driven by Lévy noise.

Synchronization transitions under fixed coupling parameters

Probability density functions of the order parameter

We fix the coupling parameters at $K_1 = 0.8$ and $K_2 = 8.0$. When noise effects are neglected, i.e., scale parameter $\sigma = 0$, the system (1) may stabilize at either $r = 0$ or $r \approx 0.82$. This bistability, as illustrated in Fig. 1, results in the $r(t)$ shown by the blue curves in Fig. 2. Under the influence of noise, the responses on $r(t)$ corresponding to different values of stability index α are represented by the orange curves in Fig. 2. Besides, Fig. 2 also illustrates the PDFs of the global order parameter $r(t)$. The transient behaviors of the $r(t)$ have been removed. We infer from each figure that each PDF in the deterministic case is not exactly the same, which is caused by randomizing the initial conditions.

From Fig. 2a, when $\sigma = 0$, $r(t)$ will eventually reach the synchronization state. Otherwise, $r(t)$ is more difficult to transition from $r = 0$ to $r \approx 0.82$, at $\sigma \neq 0$, then returns to $r = 0$ in a very short time, yielding a bimodal PDF with peaks near $r \approx 0$ and $r \approx 0.82$. In the intermediate case ($\alpha = 1.4$), shown in Fig. 2b, the system (1) exhibits rare and noise-induced synchronization spikes, illustrating how heavy-tailed perturbations can both suppress and transiently restore coherent behavior. The PDF, therefore, combines a dominant peak at $r \approx 0$ with a small secondary peak near $r \approx 0.82$. We observe a qualitatively similar transition for a wider range of α and σ, as detailed in the Supplementary Information (see Supplementary Note 2 and Fig. S2).

It is worth noting that for finite-size systems (e.g., $N = 100$), intrinsic fluctuations can induce spontaneous transitions from an incoherent to the synchronized state in the bistable region[39]. In this regime, our simulations at $N = 100$ show that the presence of Lévy noise counteracts such finite-size-induced synchronization and keeps the order parameter in a low-synchronization regime. To examine how this behavior depends on the system size, we further increase the ensemble size to $N = 200$ and $N = 500$. For these larger networks, where intrinsic finite-size fluctuations are strongly reduced, and the deterministic dynamics already remain incoherent, the addition of Lévy noise does not generate global synchronization (see Supplementary Note 2 and Fig. S3). Taken together, these observations indicate that the desynchronizing influence of impulsive Lévy noise in the

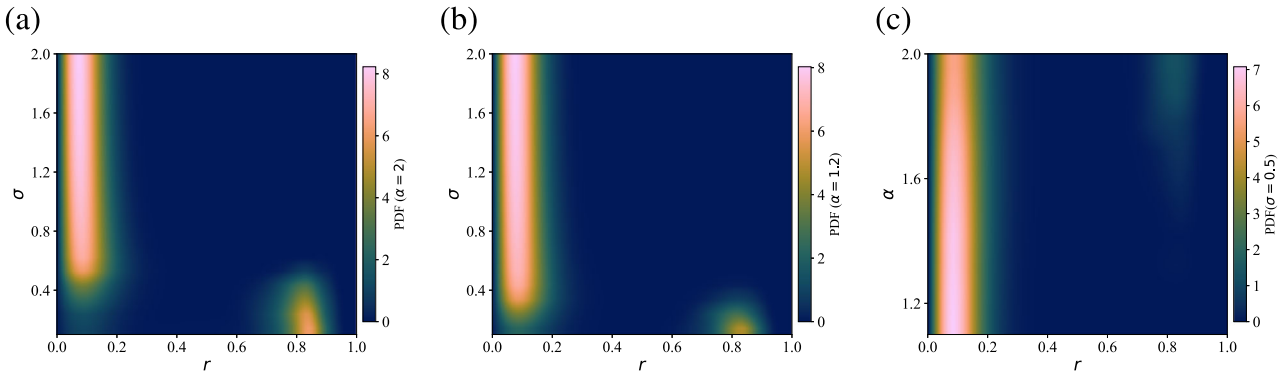

Fig. 3 | The PDF under different stability index and scale parameter. σ and α are scale parameter and stability index, respectively. The horizontal axis is the order parameter r, the vertical axis is the σ and α, and different colors represent PDF values. **a** $\alpha = 2$. **b** $\alpha = 1.2$. **c** $\sigma = 0.5$.

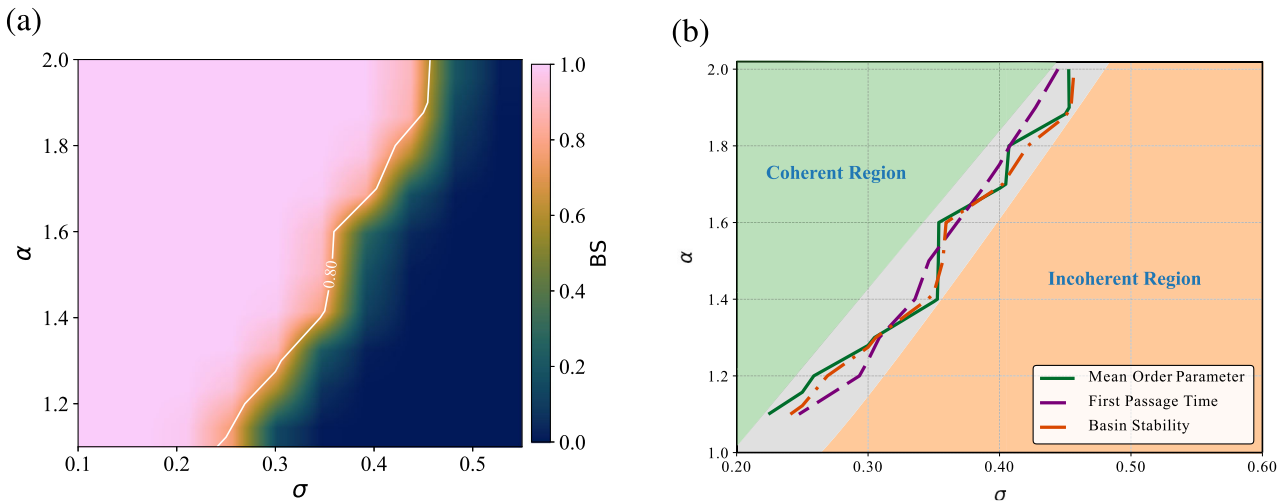

Fig. 4 | Heatmap of three metrics under different stability index and scale parameters. σ denotes the scale parameter, and α represents the stability index. **a** Basin stability BS. Dark blue denotes BS ≈ 0, where almost no initial conditions synchronize. While pale pink denotes BS ≈ 1, nearly all trajectories synchronize. The white curve is the contour line, marking the region with BS = 0.8. **b** Phase diagram in the (σ, α) plane summarizing three indicators. The green region corresponds to the coherent regime, the orange region corresponds to the incoherent regime, and the gray band marks the transition region. The solid green curve shows the transition boundary estimated from the mean order parameter $\langle r \rangle$, the purple dashed curve shows the boundary estimated from the MFPT T_{first}, and the red dash-dotted curve shows the boundary given by the basin-stability criterion BS.

bistable region is consistent over the range of system sizes considered here, although a systematic finite-size scaling analysis of basin boundaries is beyond the scope of the present work.

Therefore, as α decreases, the same σ both more readily suppresses persistent synchronization and occasionally gives rise to transient coherence events. Whereas moderate Gaussian fluctuations can still drive the network from incoherence into synchrony, Lévy noise shifts the balance toward desynchronization.

Furthermore, we consider the PDFs under different α and σ. Figures 3a, b visualize how the stationary PDF of the order parameter r is reshaped by σ. We plot the joint density $P(r, \sigma)$ for two fixed values of the stability index ($\alpha = 2$ and $\alpha = 1.2$), while panel c shows $P(r, \alpha)$ at a fixed $\sigma = 0.5$. We find that, in each subfigure, two high-density regions appear, one near $r \approx 0.1$ (the incoherent attractor), and one near $r \approx 0.82$ (the synchronized attractor).

As α decreases from 2.0 to 1.2, the incoherent peak both broadens in σ and loses weight relative to the synchronized peak, namely, heavy-tailed fluctuations progressively erode the stability of the synchronized branch. Besides, as the decrease of α, σ required to suppress synchronization decreases accordingly. Figures 3a, b verify them. We also provide the PDFs under $\sigma = 0.5$ in Fig. 3c. The system (1) mainly focuses on the incoherent state, i.e., $r \approx 0$. Therefore, the critical value of α needs to be determined based on the different values of σ. However, no matter what the value of α is, $\sigma > 0.5$ will basically not result in synchronization. The PDF for the case of $\alpha = 1.8$, presented in Fig. S5 (Supplementary Note 3), further corroborates this phenomenon. In the subsections that follow, we will systematically quantify these phenomena in terms of the mean order parameter, mean first-passage times, and basin stability, to map out the critical boundary (α_c, σ_c) beyond which synchronization is suppressed. When $\alpha < 1$, the first-order moment of Lévy noise does not exist, and, hence, we do not consider the case of $\alpha < 1$ here.

Basin stability and quantitative analysis of the synchronization transition

The results of basin stability BS (defined in the "Methods" section) are shown in Fig. 4a under different σ and α. We observe that, at fixed σ, increasing α raises BS. In other words, when the noise has lighter tails, it is less effective at preventing synchronization. By contrast, for smaller α, BS drops more rapidly, indicating that rare large jumps more easily trap the sytem (1) in the incorherent basin. Besides, at fixed α, increasing σ monotonically decreases BS. Once σ exceeds the white line, the majority of initial conditions fail to reach synchronization within the observation window. In practice, this means that Gaussian-like fluctuations require a larger σ to suppress synchronization than heavy-tailed Lévy fluctuations do.

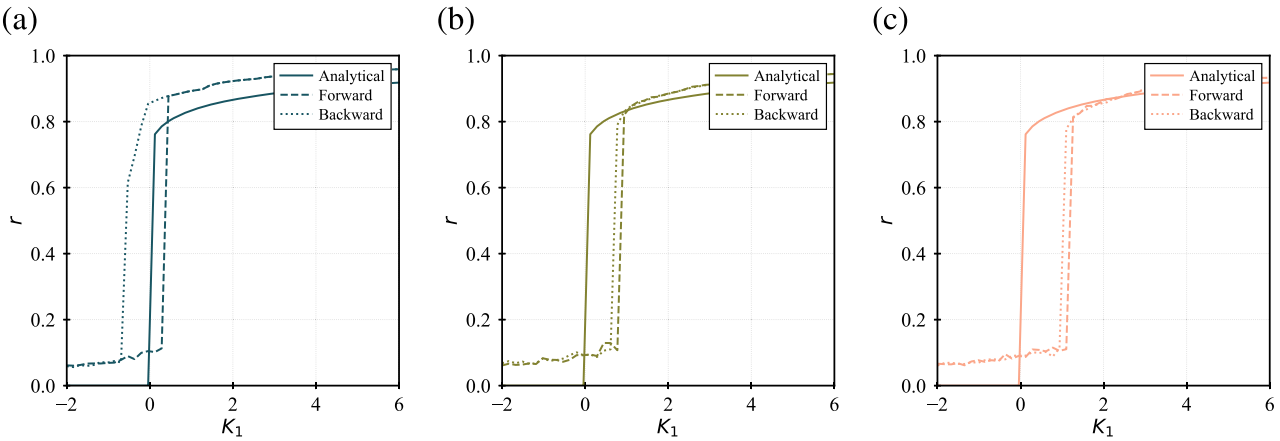

Fig. 5 | Bifurcation structure across coupling and noise parameters. The solid line is the solution to Eq. (4). Forward numerical iterations are denoted by long dashed lines with dots, while backward numerical iterations are denoted by short dashed lines. **a** The deterministic case, $\alpha = 2$, $\sigma = 0$. **b** The Gaussian case, $\alpha = 2$, $\sigma = 0.5$. **c** The Lévy noise, $\alpha = 1.6$, $\sigma = 0.5$. Here, K_1 is the pairwise coupling strength, α is the stability index, and σ is the noise scale parameter.

Furthermore, the mean of the order parameter $\langle r \rangle$ (defined by the "Methods" section) and the mean first-passage time (MFPT) T_{first} (illustrated by the "Methods" section) distribute at the similar transition region, including coherent and incoherent regions. The full results are provided in Fig. S6 (Supplementary Note 4). To quantitatively characterize this transition, we simultaneously analyze three metrics, including BS, $\langle r \rangle$, and T_{first}, with the results synthesized in Fig. 4b. We find that the three contour critical curves have overlapping regions but are not identical. The discrepancy arises because the three indicators measure the dynamical behaviors from different perspectives, including the mean order parameter, the escape time, and the size-volume of the basin. Even though the same threshold criteria are applied, the indicators focus on different aspects, leading to boundary deviations. Therefore, we define the largest region covered by the overlapping segments of the three curves as the transition region. Within this region, BS and $\langle r \rangle$ may not simultaneously exceed 0.8 under the same parameters, and T may not necessarily increase beyond $T_{\max}$. Consequently, synchronization occurs in the green region, but is suppressed in the yellow region, and synchronization in the transition region depends on specific conditions.

The above analysis illustrates the synchronization dynamics of system (1) under Lévy noise excitation at fixed coupling parameters K_1 and K_2. Specifically, as the stability index α decreases, synchronization becomes increasingly suppressed. Furthermore, when the scale parameter σ exceeds 0.5, synchronization is suppressed. We validate these conclusions through heatmap analyses of the mean order parameter, the mean first-passage time, and the basin stability.

Modulation of synchronization by coupling parameters

Bifurcation hysteresis

In the following, varying K_1 is investigated. We set $K_2 = 8$ to describe the transition process. Figure 5 illustrates r versus the first-order coupling K_1. The solid curve is the analytical solution of Eq. (4), the long-dashed line with dots is the forward numerical simulation, i.e., increasing K_1. The short-dashed line is the backward simulation, i.e., decreasing K_1.

Figure 5a refers to the deterministic case. A clear hysteresis loop opens, signifying bistability between the incoherent and synchronized states. The Gaussian and Lévy noise cases are compared in Fig. 5b and c. In both stochastic cases, the overall bifurcation structure is preserved, but the curves shift to larger values of K_1, reflecting the extra coupling parameter needed to overcome noise and achieve synchrony. In addition, the case with Gaussian noise depicted in Fig. 5b shows a relatively small rightward shift, whereas the Lévy noise case in Fig. 5c exhibits a more pronounced shift to the right. In addition, we also generate bifurcation diagrams for different K_2, as shown in Fig. S7 (Supplementary Note 5).

While the results presented above are obtained for $N = 100$, we verify that the suppression effect of Lévy noise and the overall hysteresis structure are robust to system size. Additional simulations performed with $N = 200$ and $N = 500$ show qualitatively similar behaviors, specifically the enhanced suppression under Lévy noise, verifying that the observed transitions are not finite-size artifacts. Detailed comparisons for larger system sizes are provided in Fig. S8 (Supplementary Note 5).

Integrated analysis of three metrics

Furthermore, we now consider the BS, the mean order parameter, and MFPT under varying K_1 and K_2. Figure 6 shows the BS as a function of K_1 and K_2 under different types of noise. In the deterministic case, the incoherent state dominates for low K_1 and low K_2, i.e., BS = 0. Once K_1 and K_2 jointly exceed a boundary, the synchronization captures essentially the entire state, i.e., BS = 1. Considering Gaussian noise, in Fig. 6b, adding moderate white noise fluctuations shifts the transition region to larger values of K_1 and K_2. In other words, stochastic perturbations make the synchronization less resilient. Besides, in Fig. 6c, Lévy noise further reduces the resilience of the synchronization regime.

Furthermore, $\langle r \rangle$ and the MFPT T_{first} in the (K_2, K_1) plane are shown in the Figs. S9 and S10 (Supplementary Note 6), showing that Lévy noise further shrinks the high-coherence region (with a fuzzier boundary), and that T_{first} exhibits a clear boundary and is systematically larger under Lévy noise than under Gaussian noise for the same (K_2, K_1).

Therefore, noise transforms the deterministic bistable transition into a broad crossover region. Gaussian fluctuations blur the boundary, but still allow an extensive region of synchronization. In contrast, Lévy fluctuations not only blur but also shift this boundary, requiring stronger coupling to reach synchronization.

Finally, to ensure that the observed suppression of synchronization is a robust physical feature rather than a finite-size artifact, for example, we extend the results of the mean order parameter to larger system sizes ($N = 200$ and $N = 500$). As detailed in the Fig. S11 (Supplementary note 7), the qualitative landscape remains consistent across system sizes: the synchronized region is invariably smaller, and the transition boundary is shifted to higher coupling strengths under Lévy noise compared to the Gaussian case. This demonstrates that the dominance of heavy-tailed fluctuations in suppressing global coherence is intrinsic to the noise distribution and persists toward the thermodynamic limit.

Spike statistics and spectral analysis

As demonstrated in the above sections, the system (1) exhibits transitions between incoherence and synchronization. Particularly under the influence of Lévy noise, such transitions occur repeatedly and

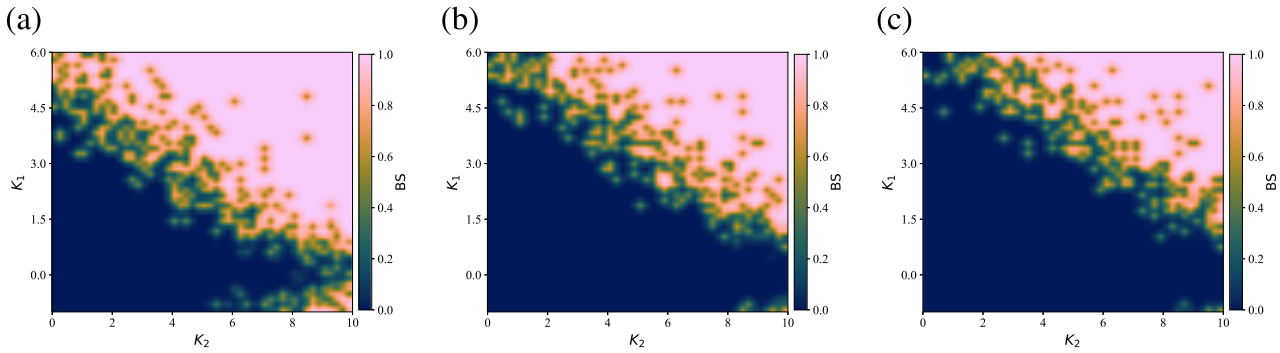

Fig. 6 | Basin-stability maps across pairwise and higher-order coupling strengths. Here, BS denotes basin stability, K_1 is the pairwise coupling strength, and K_2 is the higher-order coupling strength. σ and α denote the scale parameter and stability index, respectively. **a** The deterministic case. $\sigma = 0$. **b** The Gaussian case. $\alpha = 2$ and $\sigma = 0.5$. **c** The Lévy case. $\alpha = 1.6$ and $\sigma = 0.5$. The basin stability in the Gaussian case is similar to the deterministic case. The Lévy noise case shows a significant shrinkage of the high BS, indicating a much stronger destabilizing effect on the synchronization state.

intermittently, driving the system (1) to alternate rather unpredictably between synchronization and incoherence. These intermittent and abrupt transitions can be regarded as extreme events in the dynamical system[41]. Therefore, it is important to analyze the frequency and characteristics of these recurrent extreme events, capturing the complex interplay between synchronization and incoherence.

Spike amplitude and the number of spikes

Here, a spike or an extreme event refers to a short excursion of the order parameter $r(t)$ above a critical threshold r_{critical}. We quantify these spikes using two metrics: amplitude and frequency (see the "Methods" section for the precise definitions). The results of maximum spike amplitude $R_{\max}(\alpha, \sigma)$ and spike count $N_{\text{spikes}}(\alpha, \sigma)$ are shown in Fig. 7.

Figure 7a depicts the averaged results of $R_{\max}(\alpha, \sigma)$ by multiple trajectories for different α and σ. It is worth noting that these averaged results are taken only when exceeding r_{critical}, rather than each amplitude. We observe that when σ is large, synchronization is suppressed completely, resulting in no spikes. In contrast, when σ is small, $R_{\max}(\alpha, \sigma)$ becomes relatively large. These trends are displayed in Fig. 7c. Although there are small fluctuations around $\sigma \in [0.6, 0.8]$, $R_{\max}(\alpha, \sigma)$ exhibits an overall decreasing trend as σ increases. Moreover, larger α are associated with a slower decline of $R_{\max}(\alpha, \sigma)$, whereas smaller α produce a faster decrease. Figure 7d shows that $R_{\max}(\alpha, \sigma)$ increases with α. This increase is stronger at larger σ and negligible at small σ. These results illustrate the effect of Lévy noise on the maximum spike amplitude under different α and σ. In particular, smaller α as well as larger σ promote stronger suppression of spikes. Figure 7b shows the $N_{\text{spikes}}(\alpha, \sigma)$ for different α and σ. Similar to Fig. 7a, $N_{\text{spikes}}(\alpha, \sigma)$ is highest when σ is small and α is large, and vice versa. Moreover, when σ is sufficiently large, the system (1) does not undergo transitions, resulting in no spikes. Besides, Fig. 7e shows a detailed $N_{\text{spikes}}(\alpha, \sigma)$ under different α. We observe that $N_{\text{spikes}}(\alpha, \sigma)$ consistently decreases as σ increases. Thus, a smaller σ corresponds to larger $N_{\text{spikes}}(\alpha, \sigma)$. $N_{\text{spikes}}(\alpha, \sigma)$ under different σ are shown in Fig. 7f. With increasing α, $N_{\text{spikes}}(\alpha, \sigma)$ either remain nearly constant or gradually increase. $N_{\text{spikes}}(\alpha, \sigma)$ attains higher values for larger α. Therefore, the system (1) always exhibits more frequent spikes when α is larger and σ is smaller.

To disentangle the effects of tail heaviness from that of the overall intensity, we also analyze the spikes in the (α, D) plane. In this analysis, the scale is chosen as $\sigma = D^{1/\alpha}$, so that $D = \sigma^{\alpha}$ keeps constant. The resulting heatmaps $R_{\max}(\alpha, D)$ and $N_{\text{spikes}}(\alpha, D)$ are shown in Fig. 8. These plots reveal that both the $R_{\max}(\alpha, D)$ and $N_{\text{spikes}}(\alpha, D)$ decrease monotonically with D. Whereas for fixed D, their dependence on α is much weaker than their variation with D. This indicates that the effective noise intensity D is the primary control parameter for the spiking behavior, while the Lévy index α provides only a secondary modulation at constant D.

Autocorrelation and power spectrum analysis of spikes

Moreover, analyzing only the amplitude and number of spikes is insufficient to fully characterize the impact of Lévy noise on synchronization transitions in the system. Therefore, we further explore the intrinsic temporal structural features of the spike sequences. Using the edit distance method[42], we compute the autocorrelation function in the time domain and the power spectrum in the frequency domain of the spike sequences.

Spike sequences are discrete and irregularly spaced, and occasionally have large intervals. Therefore, it is difficult to directly calculate the autocorrelation function and power spectrum. We use the statistical properties of the autocorrelation function (EDACF) and power spectral estimate (EDSPEC) based on the edit distance[43]. The main idea behind the edit distance method is to quantify how similar two sequences of symbols or events are by calculating the smallest number of operations needed to turn one sequence into the other. These steps include adding, removing, and moving symbols[44].

We select representative points from three distinct regions in Fig. 4b to investigate the autocorrelation and power spectra of the corresponding spike sequences. Specifically, the coherent region is characterized by $\alpha = 1.6$, $\sigma = 0.3$ (Fig. 9a and b), the transition region by $\alpha = 1.4$, $\sigma = 0.33$ (Fig. 9c and d), and the incoherent region by $\alpha = 1.4$, $\sigma = 0.4$ (Fig. 9e) and f). The blue and red shaded regions represent one standard error of the mean (SEM), while the black curves indicate the 95% confidence levels (see the "Methods" section).

We observe from Fig. 9a that the EDACF decays to zero at approximately lag values greater than 100, whereas in Fig. 9c the EDACF decays more rapidly, reaching zero at lag values smaller than 100. In Fig. 9e, the EDACF reaches zero at around lag ≈ 100. These findings indicate that spike sequences in the coherent region display the longest-lasting serial dependency, whereas sequences in the incoherent region exhibit the shortest temporal correlations. Furthermore, from Fig. 9b, d, and f, the spike sequences consistently follow a power-law $f^{-0.951}$, $f^{-0.930}$, and $f^{-0.849}$, respectively. Then we give the hypothesis: H_0: The temporal structure of the observed event sequence is indistinguishable from that of a random process, implying the absence of periodicity or long-range correlation. H_1: The event sequence exhibits a significant non-random temporal structure, such as periodicity, long-range correlation, or notable autocorrelation (see the "Methods" section). If the EDSPEC of the actual data exceeds these thresholds at certain frequencies at the 95% confidence level, we reject the null hypothesis, indicating a significant non-random temporal structure in the system (1). Specifically, the EDSPEC in Fig. 9d and f remains within the 95% confidence level, indicating no significant periodicities. However, there are peaks in the EDSPEC in Fig. 9b, which exceed the 95% confidence level, indicating the existence of real but small spectral peaks.

To quantify the decay of the ensemble-averaged EDSPEC and to assess whether a power-law is an appropriate model, we fit a power law $P(f) \propto$

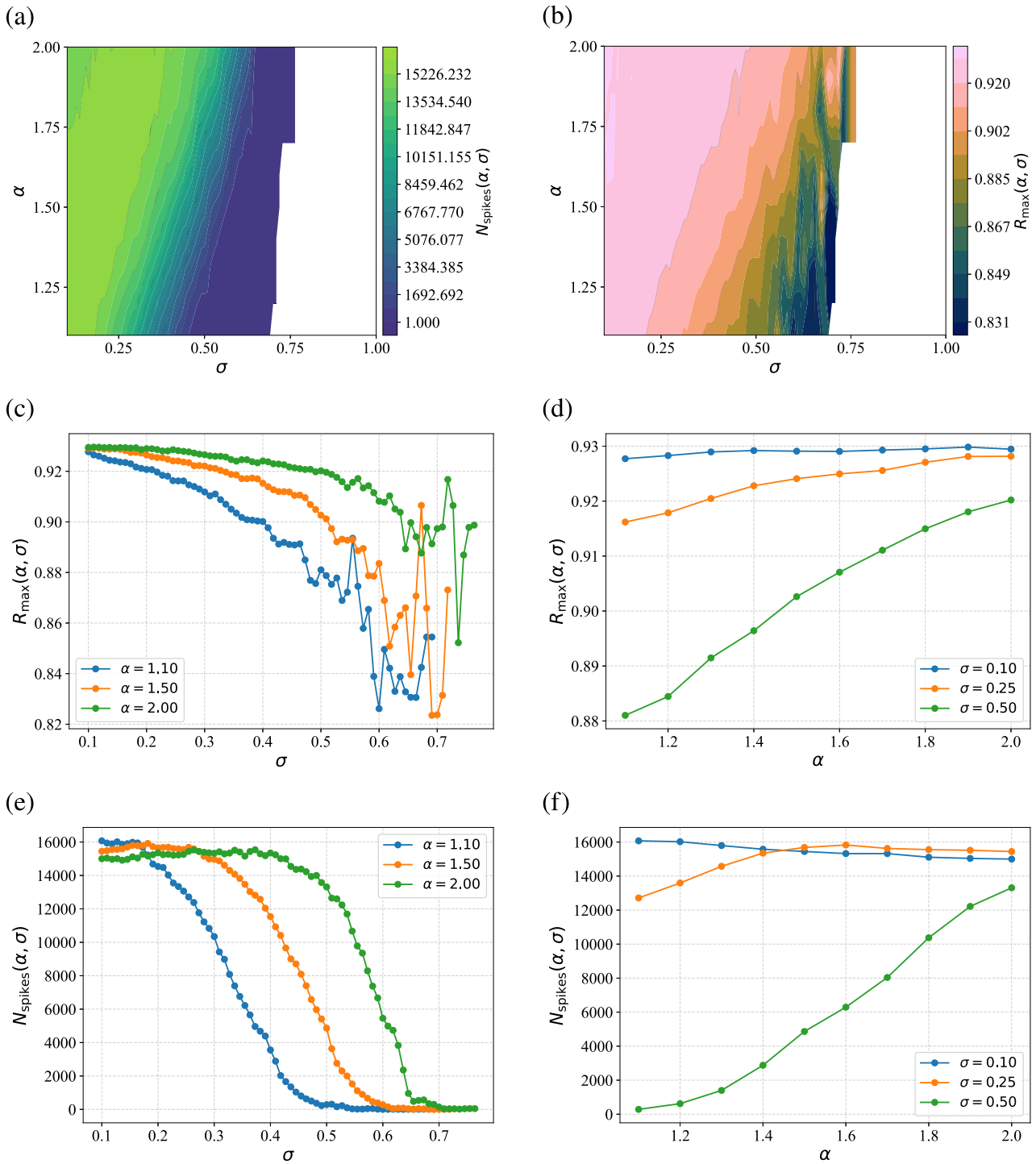

Fig. 7 | Dependence of maximum spike amplitude and spike count on the scale parameter and the stability index. a The maximum spike amplitude $R_{max}(\alpha, \sigma)$. The thin curves overlaying the color map are contour lines of $R_{max}(\alpha, \sigma)$, i.e., they connect the stability index and the scale parameter (α, σ) with the same $R_{max}(\alpha, \sigma)$. Blank regions indicate no spikes occurred. **b** The spike count $N_{spikes}(\alpha, \sigma)$. The thin curves are contour lines of $N_{spikes}(\alpha, \sigma)$. Blank regions also indicate that no spikes occurred. **c** The $R_{max}(\alpha, \sigma)$ is plotted as a function of σ for different α. **d** $R_{max}(\alpha, \sigma)$ is plotted as a function of α for different σ. **e** $N_{spikes}(\alpha, \sigma)$ as a function of σ. Different colors correspond to different values of the parameter α. **f** $N_{spikes}(\alpha, \sigma)$ plotted against α. Curves with different colors correspond to different σ.

$f^{-\beta_{pow}}$ to the part of the ensemble-averaged spectrum that appears approximately linear in log-log coordinates. For comparison, we also fit a simple exponential model in log-linear form, $\log_{10} P(f_i) = A + Bf_i$, to the same frequency range and compute the Akaike information criterion (AIC) for both models[45]. For all parameter sets considered, the power-law fits yield the weighted coefficient of determination $R^2 \approx 0.99$, and the AIC of the power-law model is lower than that of the exponential model by $\Delta\text{AIC} \sim 10^4$. Since $\Delta\text{AIC} \gg 10$ is commonly interpreted as very strong evidence in favor of a model with a smaller AIC, this strongly prefers the power-law description over the exponential alternative in the frequency range studied (see Table S1 for detailed numerical values in the Supplementary Note 8).

Considering spike sequences characterized by large inter-event intervals, it becomes more meaningful to analyze these sequences by segmenting them into shorter windows. Thus, we present the EDACF and EDSPEC

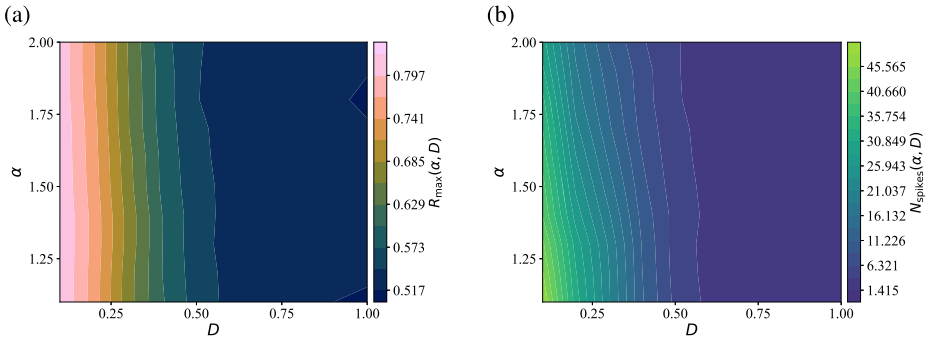

Fig. 8 | Influence of noise intensity and stability index on the maximum spike amplitude and spike count. a Heatmap of the maximum spike amplitude $R_{max}(\alpha, D)$ under different α and D. The thin curves denote contour lines of $R_{max}(\alpha, D)$. **b** Heatmap of the spike count $N_{spikes}(\alpha, D)$. The thin curves are contour lines of $N_{spikes}(\alpha, D)$.

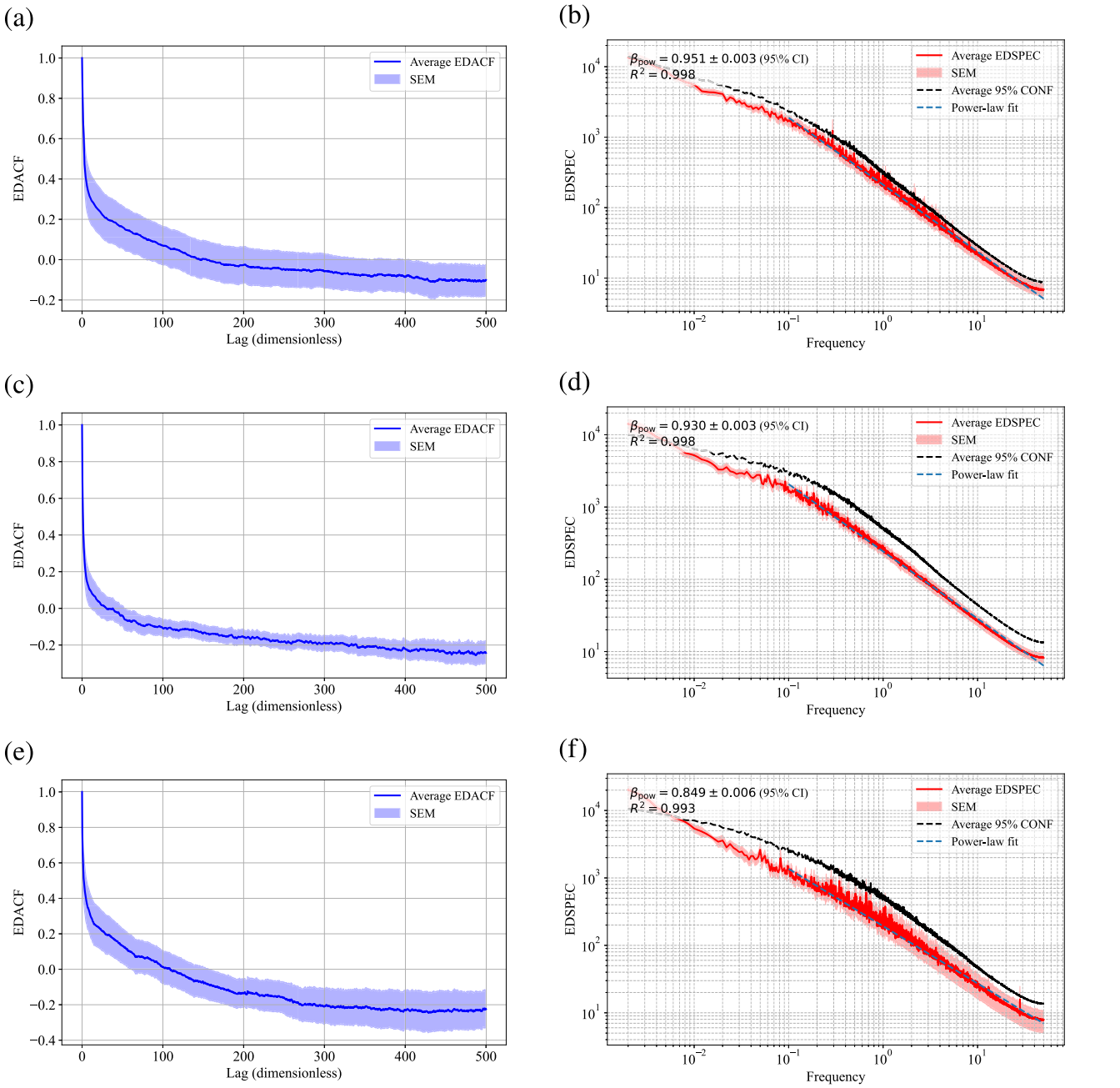

Fig. 9 | Autocorrelation and spectral analysis of spike sequences under different noise conditions. a, **b** $\alpha = 1.6$, $\sigma = 0.3$. **c**, **d** $\alpha = 1.4$, $\sigma = 0.33$. **e**, **f** $\alpha = 1.4$, $\sigma = 0.4$. **a**, **c**, **e** Estimated autocorrelation function (EDACF). The blue shaded region in EDACF indicates the standard error of the mean (SEM). **b**, **d**, **f** Estimated power spectrum (EDSPEC). EDSPEC on a log-log scale. The red shaded region also represents the SEM, while the black and green dashed lines show the 95% confidence level and the least-squares fit to a suitable range, respectively.

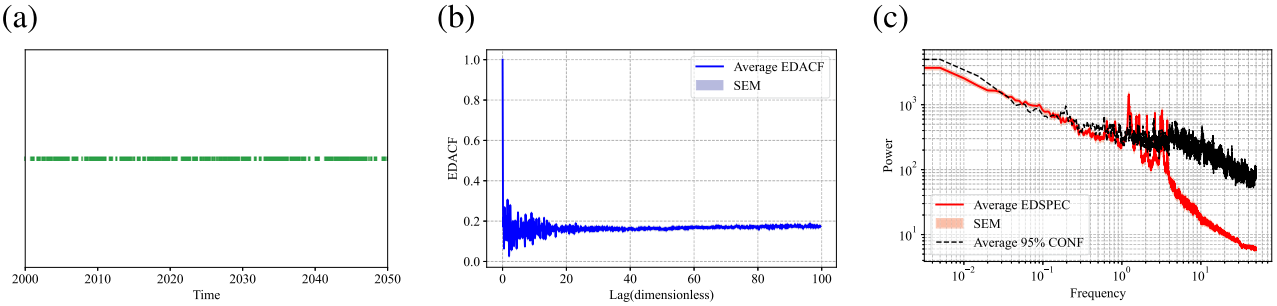

Fig. 10 | Analysis of spike sequences segmented into multiple windows. $\alpha = 1.1$ and $\sigma = 0.1$. **a** The segment of the spike sequence after window segmentation. **b** Window-averaged estimated autocorrelation function (EDACF), with shading indicating the standard error of the mean (SEM). **c** Window-averaged estimated power spectrum (EDSPEC) on a log-log scale, also displaying SEM as a shaded area. The black curve shows the 95% confidence level.

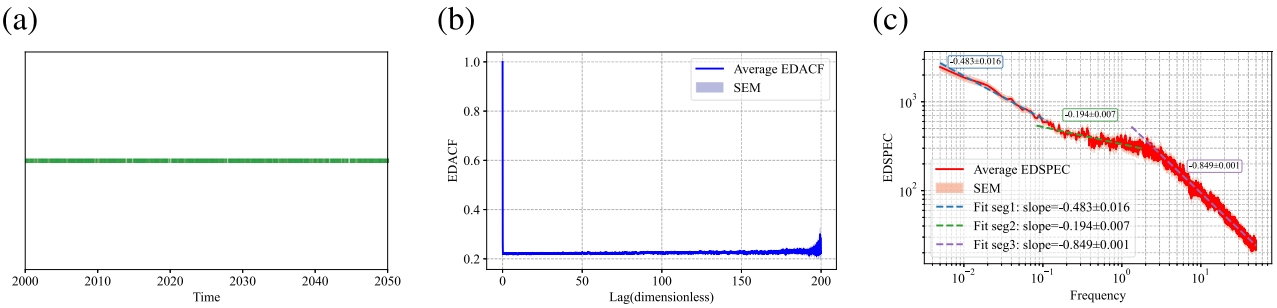

Fig. 11 | Analysis of Lévy noise spike sequences using window segmentation. $\alpha = 1.1$ and $\sigma = 0.1$. **a** Segment of the spike sequences extracted from Lévy noise. **b** Window-averaged estimated autocorrelation function (EDACF), with standard error of the mean (SEM) indicated by shading. **c** Window-averaged estimated power spectrum (EDSPEC) on a log-log scale, also with SEM depicted by shading. The three dashed lines are the fitted curves for the three frequency bands, respectively.

calculated for windowed spike segments, allowing us to examine the temporal variations and local characteristics within the spike sequences in more detail. We assume that spikes are grouped into sequences if intervals between spikes exceeded a threshold $I_{\text{threshold}} = 200$. Each segment is, thus, bounded by intervals greater than $I_{\text{threshold}}$. Then the EDACF and EDSPEC are calculated independently within each window. Taking the case of $\alpha = 1.1$ and $\sigma = 0.1$ as an example, the averaged EDACF and EDSPEC results from multiple segmented windows are shown in Fig. 10.

Figure 10a shows an example segment of spikes over a time window, illustrating the discrete and irregular spikes. Figure 10b shows the averaged EDACF computed by multiple segmented windows. The EDACF decays rapidly from an initial lag and stabilizes at a relatively low value, indicating limited long-range autocorrelation across spike events. Shaded regions represent the SEM. It means that the averaged EDACF lies entirely within the shaded SEM regions, indicating a high consistency across segmented windows. Thus, the observed spike dynamics are robust. Figure 10c displays the averaged EDSPEC, which reveals a power-law behavior at lower frequencies, followed by distinct peaks at higher frequencies. Besides, multiple clear peaks exceed the 95% confidence level, which was established based on a null model of random spiking activity. This result allows us to reject the null hypothesis, confirming that the observed oscillations are statistically significant. The low variability, demonstrated by the SEM completely encompassing the EDSPEC curve, further indicates the presence of robust, spike-like structures. Of course, we test on multiple trajectories to obtain EDACF and EDSPEC, showing similar phenomena.

For comparison, we also present the Lévy sequence, along with the estimated EDACF and EDSPEC. However, the previously threshold r_{critical} is unsuitable for this Lévy sequence. We adopt the 80% percentile as an appropriate threshold to obtain spikes. Similarly, we divide the sequence into windows of length 200 to obtain the series shown in Fig. 11a, the spike sequence appears relatively uniform. Hence, we directly apply the edit distance to estimate the average EDACF and EDSPEC across multiple windows. The results are illustrated in Fig. 11b and c, respectively. EDACF shows a sharp initial peak rapidly decreasing to a consistently low level. It indicates that the spikes generated by Lévy noise exhibit rather weak correlations. When the lag is large, the fluctuation is small. In Fig. 11c, EDSPEC shows a steady declining power spectrum, highlighting that Lévy noise exhibits low-frequency behavior with a simple monotonic decay. In addition, we fit three frequency bands in Fig. 11c. All three bands show a power law decay, with $f^{-\beta_1}, f^{-\beta_2}$, and $f^{-\beta_3}$. $\beta_1 = 0.483$, $\beta_2 = 0.194$, and $\beta_3 = -0.849$, which indicates long-range correlation and stationarity. Furthermore, we check that the results are robust with respect to the precise choice of the spike threshold for the Lévy noise (70% and 90% percentile yield similar EDACF and EDSPEC curves, shown in Fig. S12 (Supplementary Note 9)).

To demonstrate the fundamental difference in temporal correlation between the collective dynamics of the system (1) and the Lévy noise, we compare the spike interval distributions of the order parameter $r(t)$ and $\zeta_i(t)$. The distribution for the spike sequences of $r(t)$ exhibits a clear power-law decay over several orders of magnitude (Fig. 12a). This behavior is a hallmark of long-range correlations, indicating that events in the system's output are not independent but possess a long memory. In contrast, the interval distribution for $\zeta_i(t)$ decays much faster than a power law, showing a progressively steeper slope on a log-log scale (Fig. 12b). This demonstrates a lack of long-range correlation. Therefore, this comparison reveals that the complex, long-memory dynamics observed in the system (1) are an emergent property, rather than a simple reflection of the input noise characteristics.

Discussion

Our findings reveal that Lévy noise-induced dynamics are qualitatively distinct from the standard Gaussian dynamics. Previous investigations show that Gaussian noise in higher-order systems acts as a diffusive force, gradually eroding a synchronized state or shifting its critical point. Gaussian noise may also stabilize dynamics near the Ott-Antonsen manifold[33] or

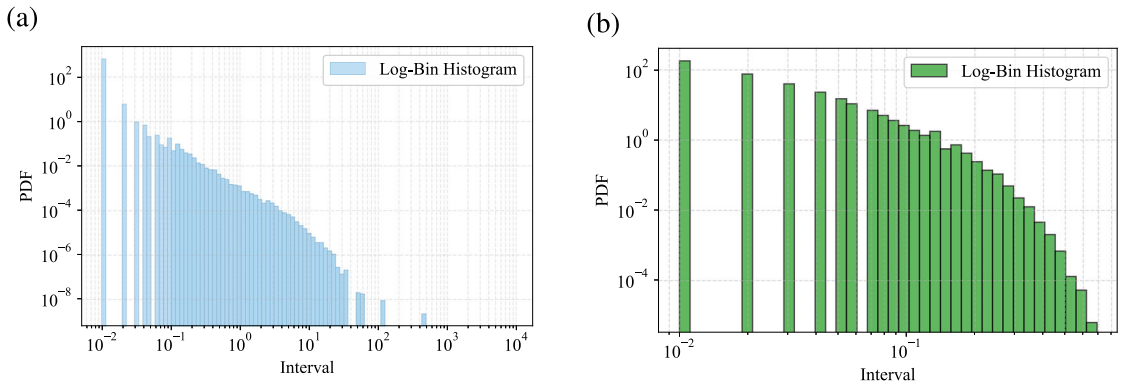

Fig. 12 | PDFs of spike intervals for system (1). a The histogram of spike intervals combined with short intra-window intervals and longer inter-window intervals. A power-law fit characterizes the heavy-tailed behavior. **b** The PDF of spike intervals, without requiring window segmentation due to shorter inter-spike intervals.

smooth abrupt transitions into continuous ones[34]. In sharp contrast, our results demonstrate that the heavy-tailed jumps of Lévy noise are non-perturbative. They not only erode coherence but also provide instantaneous and powerful kicks that actively suppress synchronization by destroying emerging clusters. This leads directly to the core observation of our work, i.e., the generation of extreme spikes.

Furthermore, our analysis uncovers an active suppression of synchronization by Lévy noise that contrasts with classic noise-induced transitions. This active suppression is a key to understanding the system's behavior. To clarify the role of finite-size effects, we have compared deterministic and Lévy-driven dynamics for different system sizes. For moderate system sizes, the noise-free dynamics can exhibit rare, finite-size-induced transitions from an incoherent to a synchronized state. In this regime, the introduction of Lévy noise counteracts such transitions and prevents the system from remaining in a highly synchronized state, showing that the observed suppression is not solely a consequence of intrinsic fluctuations. For systems of a larger size, finite-size-induced transitions become almost negligible. In these cases, the deterministic dynamics are already incoherent, and adding Lévy noise fails to induce synchronization, maintaining its desynchronizing role. Taken together, these observations indicate that the desynchronizing influence of heavy-tailed Lévy noise in the bistable region is robust over the range of system sizes. In the synchronized state, the spikes are not random and isolated events. As revealed by our quantitative analysis using the edit distance method, these spikes suggest a residual and transient form of local organization. The quasi-periodic nature suggested by the spike-like structure could correspond to a characteristic timescale of this formation-and-destruction process of transient synchronous clusters.

This suppression mechanism is not merely a modeling curiosity but suggests a general principle, offering a potential mechanism for preventing runaway synchronization and epileptic seizures, as well as a dynamical explanation for polarization in socioeconomic systems. Hypersynchronization is often linked to pathological states like epilepsy[46,47]. The brain also employs powerful mechanisms to maintain a healthy, desynchronized state essential for complex computation. Our model could be interpreted as a representation of such a regulatory mechanism. The higher-order connections represent complex neural assemblies, while Lévy-like excitations could model strong, disruptive external stimuli or internal channel noise. Thus, the noise-induced suppression of synchronization could be a protective feature, preventing runaway synchronization and seizures. The observed spikes might then correspond to transient, localized neural computations that are performed without triggering pathological global synchronization.

Besides, consensus formation in social groups or stability in financial markets often relies on complex, many-body interactions[48]. Our findings suggest that in the presence of randomly recurring major shocks, such as political scandals and market crashes, it becomes extremely difficult to form and maintain a global consensus or stable state. The system thus remains trapped in a desynchronized regime. Within this state, only transient, small-scale spikes could form before being shattered by the next crisis, offering a dynamical explanation for the persistent polarization or volatility seen in real systems under stress.

Of course, there are several limitations in this study. Firstly, we conduct on a network with a simplified topology. The interplay of complex topologies, such as random network or small-world network, with higher-order structures and Lévy noise remains to be explored. Secondly, the parameters of the Lévy noise are explored in a fixed range. Exploring a wider range of parameters could reveal more complex dynamical phenomena.

Therefore, future work could proceed in several directions. A systematic investigation across the full parameter space of Lévy noise is needed to map out synchronization behaviors. Implementing the model on empirical higher-order networks, such as brain connectomes or collaboration networks, would be a critical step toward validating our theoretical findings. Finally, a deeper analysis of the spike dynamics, using tools from time-series analysis to formally quantify their periodicity and statistical properties, would help to confirm our hypothesis regarding transient cluster formation and provide a richer understanding of the complex behaviors.

Conclusion

In this paper, we investigate the synchronization and spike dynamics of a higher-order Kuramoto model driven by Lévy noise. First, we analyze fixed coupling parameters K_1 and K_2, which correspond to pairwise and higher-order interactions, respectively, and identify how Lévy noise parameters significantly affect synchronization. Specifically, synchronization becomes suppressed as the Lévy stability index α. Moreover, synchronization is always inhibited for a sufficiently large noise scale parameter σ, as evidenced by the basin stability, mean order parameter, and mean first-passage time. Next, by modulating K_1 and K_2, we explore bifurcation hysteresis phenomena. The presence of Lévy noise transforms sharp deterministic synchronization boundaries into broader and smoother transitions, requiring stronger coupling to achieve comparable synchronization compared to Gaussian noise. Finally, we focus on spike dynamics induced by Lévy noise, defining spikes as periods during which the order parameter exceeds a predefined threshold. We calculate the maximum amplitude and the number of spikes. Both always occur at positions with a smaller scale parameter σ. Spectrum analysis is applied by an edit distance algorithm. By comparing spike intervals and Lévy noise intervals, we further emphasize the power-law scaling introduced by higher-order Kuramoto under non-Gaussian noise.

Crucially, these results illustrate that both synchronization transitions and spike occurrences under Lévy noise can be viewed as manifestations of extreme events in oscillator networks. Synchronization transitions represent collective extreme coherence phenomena, while spike dynamics correspond to transient, highly coherent states that substantially deviate from typical dynamics. Such a unified understanding of extreme events induced by non-Gaussian noise expands our insights into synchronization dynamics,

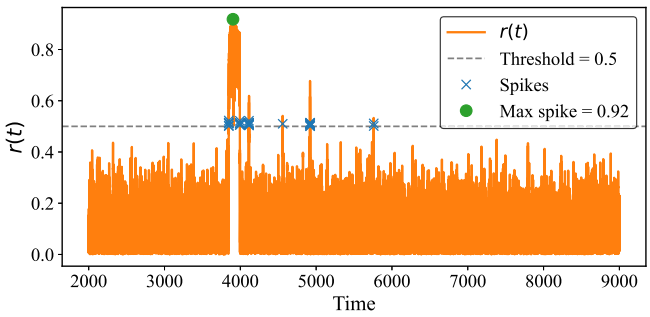

Fig. 13 | The order parameter under the stability index $\alpha = 1.4$ and scale parameter $\sigma = 0.4$. The dotted line is the threshold r_{critical}, the cross marks the spikes in a given time interval, and the green dot marks the maximum of the spike.

highlighting the critical role of higher-order interactions and Lévy-type fluctuations in governing rare but impactful dynamical behaviors. Our findings provide valuable perspectives for managing and predicting extreme events in real-world complex oscillator networks subjected to stochastic excitations.

Methods

Model parameters

For the system (1), the numerical integration is performed using the Ruge-Kutta method with a time step $dt = 0.01$. The total simulation time is set to $T = 10^6$ time units, with the initial $T_{\text{tr}} = 10^5$ discarded as transients. Since both the Lorentzian distribution of natural frequencies $g(\omega)$ and the Lévy noise distribution $L(\zeta_i(t))$ possess diverging variances, we quantify the relative noise strength using the ratio of their scale parameters. Since the scale parameter of the standard Cauchy distribution is 1, the Lévy scale parameter σ serves as a direct measure of the noise intensity relative to the intrinsic heterogeneity.

Moreover, a single finite-size realization ($N = 100$) of natural frequencies $\{\omega_i\}$ may contain extreme outliers (Histogram of $|\omega_i|$ and histogram of the sample maximum $\max_i|\omega_i|$ are shown in Fig. S13 (Supplementary Note 10)). To ensure that our results are not artifacts of atypical realizations, the macroscopic quantities reported (e.g., order parameters) are obtained by averaging over multiple independent realizations of $\{\omega_i\}$ in addition to noise trajectories.

To ensure that all numerical results correspond to the stationary regime, we discard an initial transient interval from each simulation. For each (α, σ), we integrate the dynamics up to a final time T with time step dt, and monitor the ensemble-averaged order parameter $r(t)$ as well as its running time average over sliding windows of length ΔT. Specifically, we define

$$R(t) = \langle r \rangle_{[t-\Delta T, t]},$$

denotes the time average of $r(t)$ over the interval $[t-\Delta T, t]$. Starting from early times, we increase t and determine the smallest time T_{tr} for which the change between two consecutive windows satisfies

$$\left|R(t) - R(t - \Delta T)\right| < \varepsilon.$$

We then interpret this time as the end of the transient and discard the interval $[0, T_{\text{tr}}]$ in all subsequent analyses. Throughout this work, we use $\Delta T = 20$ and $\varepsilon = 0.005$, which yields a transient length of $T_{\text{tr}} \approx 10^5$ integration steps (corresponding to $t \approx 10^3$ for $dt = 0.01$) for all parameter combinations considered. All stationary quantities are computed from data collected for $t > T_{\text{tr}}$. Furthermore, we verify that extending the integration time beyond T_{tr} (for example, by extending the simulation time to $2T$. Results are shown in Fig. S4 (Supplementary Note 2), does not affect the measured stationary observables within numerical accuracy under Lévy noise, ensuring that our conclusions are robust with respect to the precise choice of T_{tr} and T.

Deterministic reduction and order-parameter equation

In the absence of noise ($\sigma = 0$), Eq. (1) becomes deterministic and admits a low-dimensional description in terms of the order parameter. We briefly summarize the reduction and refer to Supplementary Note 11 for the detailed derivation.

Taking the thermodynamic limit $N \to \infty$, we describe the state of the system by the probability density $f(\theta, \omega, t)$ of oscillators with phase θ and natural frequency ω at time t. The density satisfies a continuity equation with phase velocity $v(\theta, \omega, t)$ obtained from Eq. (1).

Following the Ott–Antonsen ansatz[49], which has also been applied to higher-order Kuramoto interactions in ref. 39, we obtain a low-dimensional description in terms of the order parameter. Evaluating the resulting expression at the pole of $g(\omega)$ in the complex ω plane yields a closed ordinary differential equation for $r(t)$, whose explicit form is given in Eq. (4). The complete algebraic steps of the reduction are presented in Supplementary Note 11.

Order parameter and three metrics

We calculate the global order parameter $r(t)$ by Eq. (3). It can be calculated by the order parameters of multiple paths as $\langle r \rangle = \langle |N^{-1}\sum_j e^{i\theta_j}| \rangle$ and provides quantitative insights into the collective dynamics.

Basin stability is the probability that the system converges to a steady state under a specific initial condition, revealing a measure of the resilience against perturbations[50]. We obtain some initial condition samples from phase space, calculate the probability that the order parameter goes into a synchronization state experiencing long enough time.

$$\text{BS} = \frac{n_{\text{path}}}{N_{\text{path}}}, \tag{6}$$

in which n_{path} represents the number of paths going into the synchronization state, described by $r > r_{\text{threshold}}$. N_{path} is the number of all paths, and $r_{\text{threshold}} = 0.8$. If BS is large, most of the initial values in system (1) will go into the synchronization state. Otherwise, the system (1) is very sensitive to initial values and cannot go into the synchronization state. In Fig. 4b, a white contour at BS = 0.8 highlights the boundary between mostly synchronized and mostly incoherent regimes, delineating the region where at least 80% of random initial conditions end up in the synchronized state.

For the mean of order parameter $\langle r \rangle$, in Fig. 4b, the contour $\langle r \rangle = 0.8$ marks the combinations of (α, σ) at which the long-time average $\langle r \rangle$ falls below 0.8 or above 0.8. It characterizes the average synchronization or incoherence behaviors of the system (1) under noise fluctuation.

First-passage time is defined as the ensemble-averaged time at which the order parameter r first exceeds a chosen threshold $r_{\text{threshold}}$[51,52]. Specifically,

$$T_{\text{first}} = \left\langle \inf\left\{ t : r(t) > r_{\text{threshold}} \right\} \right\rangle, \tag{7}$$

where $r_{\text{threshold}}$ is the threshold we defined. According to the value of r under different states, we choose $r_{\text{threshold}} = 0.8$. When $r \geq 0.8$, the system (1) will enter the synchronization state. Besides, in Fig. 4b, we identify a threshold $T_{\text{threshold}} = 0.8T_{\text{max}}$ for MFPT, where T_{max} is the largest value of T we considered.

Spike amplitude and the number of spikes

We define a spike as a time interval during which $r(t) \geq r_{\text{critical}}$. These intervals represent sudden synchronization events[53]. Figure 13 illustrates typical responses of $r(t)$. the dashed horizontal line indicates the threshold. The blue crosses in Fig. 13 mark some spikes. The green dot highlights the spike with the maximum amplitude.

The mean-field analysis of the corresponding noise-free model in ref. 39 indicates that the unstable fixed point separating the incoherent and synchronized states is located at $r \approx 0.5$. Therefore, we set the threshold $r_{\text{critical}} = 0.5$. To provide a comprehensive framework for assessing and suppressing extreme events, we calculate the maximum amplitude of spikes and the number of spikes during the specific time interval extracted for each α and σ. The maximum spike amplitude is defined as $R_{\max}(\alpha, \sigma) = \max_{t\in[0,T]}\{r(t)|r(t) \geq r_{\text{critical}}\}$. The spike count is defined by

$$N_{\text{spikes}}(\alpha, \sigma) = \#\big\{[t_{\text{start}}, t_{\text{end}}] \subseteq [0, T] \,:\, r(t_{\text{start}}^{-}) < r_{\text{critical}},\ r(t_{\text{end}}^{+}) < r_{\text{critical}},\ r(t) \geq r_{\text{critical}}\big\}. \tag{8}$$

Edit distance algorithm

When calculating the averaged EDACF and EDSPEC, we select multiple trajectories to generate spike sequences for each parameter set. The step size of lag is 0.01. To establish the 95% confidence intervals shown, we generate 20 surrogate event sequences by randomly and uniformly redistributing events within the original observation interval. These surrogate datasets are then used to calculate the EDACF and EDSPEC, from which we derived frequency-specific thresholds corresponding to the 95% significance level. These thresholds allow a statistical comparison with the original data to test the hypotheses.

Data availability

All data needed to evaluate the findings of the paper are available within the paper.

Code availability

The Python and Julia source code is available at https://github.com/zhaodan-npu/Higher_order_kuramoto_paper_code.

Received: 26 September 2025; Accepted: 14 February 2026;
Published online: 02 March 2026

References

1. Shahal, S. et al. Synchronization of complex human networks. *Nat. Commun.* **11**, 3854 (2020).
2. Glass, L. Synchronization and rhythmic processes in physiology. *Nature* **410**, 277–284 (2001).
3. Blasius, B., Huppert, A. & Stone, L. Complex dynamics and phase synchronization in spatially extended ecological systems. *Nature* **399**, 354–359 (1999).
4. Rohden, M., Sorge, A., Timme, M. & Witthaut, D. Self-organized synchronization in decentralized power grids. *Phys. Rev. Lett.* **109**, 064101 (2012).
5. Arenas, A., Díaz-Guilera, A., Kurths, J., Moreno, Y. & Zhou, C. Synchronization in complex networks. *Phys. Rep.* **469**, 93–153 (2008).
6. Gallo, L. et al. Synchronization induced by directed higher-order interactions. *Commun. Phys.* **5**, 263 (2022).
7. Acebrón, J. A., Bonilla, L. L., Pérez Vicente, C. J., Ritort, F. & Spigler, R. The Kuramoto model: A simple paradigm for synchronization phenomena. *Rev. Mod. Phys.* **77**, 137–185 (2005).
8. Rodrigues, F. A., Peron, T. K. D., Ji, P. & Kurths, J. The Kuramoto model in complex networks. *Phys. Rep.* **610**, 1–98 (2016).
9. Strogatz, S. H. From Kuramoto to Crawford: exploring the onset of synchronization in populations of coupled oscillators. *Phys. D.* **143**, 1–20 (2000).
10. Dorfler, F. & Bullo, F. Synchronization and transient stability in power networks and nonuniform Kuramoto oscillators. *SIAM J. Control Optim.* **50**, 1616–1642 (2012).
11. Bick, C., Gross, E., Harrington, H. A. & Schaub, M. T. What are higher-order networks? *SIAM Rev.* **65**, 686–731 (2023).
12. Benson, A. R., Gleich, D. F. & Leskovec, J. Higher-order organization of complex networks. *Science* **353**, 163–166 (2016).
13. Skardal, P. S. & Arenas, A. Higher order interactions in complex networks of phase oscillators promote abrupt synchronization switching. *Commun. Phys.* **3**, 218 (2020).
14. Skardal, P. S. & Arenas, A. Abrupt desynchronization and extensive multistability in globally coupled oscillator simplexes. *Phys. Rev. Lett.* **122**, 248301 (2019).
15. Ferraz de Arruda, G., Tizzani, M. & Moreno, Y. Phase transitions and stability of dynamical processes on hypergraphs. *Commun. Phys.* **4**, 24 (2021).
16. Millán, A. P., Torres, J. J. & Bianconi, G. Explosive higher-order Kuramoto dynamics on simplicial complexes. *Phys. Rev. Lett.* **124**, 218301 (2020).
17. Xu, C. & Skardal, P. S. Spectrum of extensive multiclusters in the Kuramoto model with higher-order interactions. *Phys. Rev. Res.* **3**, 013013 (2021).
18. Kundu, S. & Ghosh, D. Higher-order interactions promote chimera states. *Phys. Rev. E* **105**, L042202 (2022).
19. Millán, A. P., Sun, H., Torres, J. J. & Bianconi, G. Triadic percolation induces dynamical topological patterns in higher-order networks. *PNAS Nexus* **3**, 270 (2024).
20. Zhang, Y., Skardal, P. S., Battiston, F., Petri, G. & Lucas, M. Deeper but smaller: Higher-order interactions increase linear stability but shrink basins. *Sci. Adv.* **10**, eado8049 (2024).
21. Albert, R., Albert, I. & Nakarado, G. L. Structural vulnerability of the North American power grid. *Phys. Rev. E* **69**, 025103 (2004).
22. Wang, S., Gu, X., Luan, S. & Zhao, M. Resilience analysis of interdependent critical infrastructure systems considering deep learning and network theory. *Int. J. Crit. Infrastruct. Prot.* **35**, 100459 (2021).
23. Bian, J., Zhou, T. & Bi, Y. Unveiling the role of higher-order interactions via stepwise reduction. *Commun. Phys.* **8**, 228 (2025).
24. Goldbeter, A. Biological rhythms: clocks for all times. *Curr. Biol.* **18**, R751–R753 (2008).
25. Dong, Y., Huo, L., Perc, M. & Boccaletti, S. Adaptive rumor propagation and activity contagion in higher-order networks. *Commun. Phys.* **8**, 261 (2025).
26. Zhao, D., Li, Y., Liu, Q., Zhang, H. & Xu, Y. The occurrence mechanisms of extreme events in a class of nonlinear Duffing-type systems under random excitations. *Chaos* **33**, 083109 (2023).
27. Wang, Z., Li, Y., Xu, Y., Kapitaniak, T. & Kurths, J. Coherence-resonance chimeras in coupled hr neurons with alpha-stable lévy noise. *J. Stat. Mech.* **2022**, 053501 (2022).
28. Zhang, X., Xu, Y., Liu, Q., Kurths, J. & Grebogi, C. Rate-dependent bifurcation dodging in a thermoacoustic system driven by colored noise. *Nonlinear Dyn.* **104**, 2733–2743 (2021).
29. Wang, Z., Xu, Y. & Yang, H. Lévy noise-induced stochastic resonance in an fhn model. *Sci. China Technol. Sci.* **59**, 371–375 (2016).
30. Campa, A. & Gupta, S. Synchronization in a system of Kuramoto oscillators with distributed Gaussian noise. *Phys. Rev. E* **108**, 064124 (2023).
31. Holder, A. B., Zuparic, M. L. & Kalloniatis, A. C. Gaussian noise and the two-network frustrated Kuramoto model. *Phys. D.* **341**, 10–32 (2017).
32. Zhao, D., Li, Y., Xu, Y., Liu, Q. & Kurths, J. Probabilistic description of extreme oscillations and reliability analysis in rolling motion under stochastic excitation. *Sci. China Technol. Sci.* **66**, 2586–2596 (2023).
33. Tyulkina, I. V., Goldobin, D. S., Klimenko, L. S. & Pikovsky, A. Dynamics of noisy oscillator populations beyond the Ott-Antonsen ansatz. *Phys. Rev. Lett.* **120**, 264101 (2018).
34. Rajwani, P. & Jalan, S. Stochastic Kuramoto oscillators with inertia and higher-order interactions. *Phys. Rev. E* **111**, L012202 (2025).
35. Marui, Y. & Kori, H. Synchronization and its slow decay in noisy oscillators with simplicial interactions. *Phys. Rev. E* **111**, 014223 (2025).
36. Zhao, D., Li, Y., Liu, Q., Kurths, J. & Xu, Y. Extreme events suppression in a suspended aircraft seat system under extreme environment. *Commun. Nonlinear Sci. Numer. Simul.* **145**, 108707 (2025).

37. Liu, Q., Xu, Y. & Li, Y. Complex dynamics of a conceptual airfoil structure with consideration of extreme flight conditions. *Nonlinear Dyn.* **111**, 14991–15010 (2023).
38. Lee, S., Kuklinski, L. J. & Timme, M. Extreme synchronization transitions. *Nature Communications* **16**, 4505 (2025).
39. Suman, A. & Jalan, S. Finite-size effect in Kuramoto oscillators with higher-order interactions. *Chaos* **34**, 101101 (2024).
40. Zan, W., Jia, W. & Xu, Y. Response statistics of single-degree-of-freedom systems with lévy noise by improved path integral method. *Int. J. Appl. Mech.* **14**, 2250029 (2022).
41. Zhao, D., Li, Y., Xu, Y., Liu, Q. & Kurths, J. Extreme events in a class of nonlinear Duffing-type oscillators with a parametric periodic force. *Eur. Phys. J.* **137**,314 (2022).
42. Banerjee, A. et al. Recurrence analysis of extreme event-like data. *Nonlinear Process. Geophys. Discuss.* **2020**, 1–25 (2020).
43. Marwan, N. & Braun, T. Power spectral estimate for discrete data. *Chaos* **33**, 053118 (2023).
44. Marwan, N. Challenges and perspectives in recurrence analyses of event time series. *Front. Appl. Math. Stat.* **9**, 1129105 (2023).
45. Akaike, H. A new look at the statistical model identification. *IEEE Trans. Autom. Control* **19**, 716–723 (2003).
46. Lepeu, G. et al. The critical dynamics of hippocampal seizures. *Nat. Commun.* **15**, 6945 (2024).
47. Li, Z. et al. Synchronization stability of epileptic brain network with higher-order interactions. *Chaos* **35**, 013137 (2025).
48. Baumann, F., Lorenz-Spreen, P., Sokolov, I. M. & Starnini, M. Modeling echo chambers and polarization dynamics in social networks. *Phys. Rev. Lett.* **124**, 048301 (2020).
49. Ott, E. & Antonsen, T. M. Low-dimensional behavior of large systems of globally coupled oscillators. *Chaos* **18**, 037113 (2008).
50. Menck, P. J., Heitzig, J., Marwan, N. & Kurths, J. How basin stability complements the linear-stability paradigm. *Nat. Phys.* **9**, 89–92 (2013).
51. Ma, J., Liu, Q., Xu, Y. & Kurths, J. Early warning of noise-induced catastrophic high-amplitude oscillations in an airfoil model. *Chaos* **32**, 033119 (2022).
52. Zan, W., Jia, W. & Xu, Y. Reliability of dynamical systems with combined Gaussian and Poisson white noise via path integral method. *Probab. Eng. Mech.* **68**, 103252 (2022).
53. Wang, Z., Yang, W., Zhang, X. & Xu, Y. Stochastic-resonance chimeras in coupled FHN neurons with α-stable lévy noise. *Phys. A* **682**, 131146 (2025).

Acknowledgements

This work is supported by the Key International (Regional) Joint Research Program of the National Natural Science Foundation (NSF) of China under Grant No. 12120101002. D. Zhao thanks the Sino-German (CSC-DAAD) Postdoc Scholarship Program.

Author contributions

D.Z. and Y.X. conceived and designed the research. D.Z. performed the main calculations and data analysis. J.K. and N.M. contributed to the development of the methodology and the interpretation of the results. D.Z. wrote the original draft of the manuscript. J.K., N.M., and Y.X. supervised the work and critically revised the manuscript. All authors discussed the results and approved the final version of the manuscript.

Competing interests

The authors declare no competing interests.

Additional information

Supplementary information The online version contains supplementary material available at https://doi.org/10.1038/s42005-026-02560-4.

Correspondence and requests for materials should be addressed to Yong Xu.

Peer review information *Communications Physics* thanks Sarika Jalan, Zhigang Zheng and the other anonymous reviewer(s) for their contribution to the peer review of this work.